



Solid acids accelerate the photocatalytic hydrogen peroxide synthesis over a hybrid catalyst of titania nanotube with carbon dot

Runyuan Ma^b, Liang Wang^{a,*}, Hai Wang^a, Ziyu Liu^c, Mingyang Xing^d, Longfeng Zhu^b, Xiangju Meng^b, Feng-Shou Xiao^{a,b,*}



^a Key Lab of Biomass Chemical Engineering of Ministry of Education, College of Chemical and Biological Engineering, Zhejiang University, Hangzhou, 310027, China

^b Key Lab of Applied Chemistry of Zhejiang Province, Department of Chemistry, Zhejiang University, Hangzhou, 310028, China

^c Key Laboratory of Low-Carbon Conversion Science & Engineering, Shanghai Advanced Research Institute, Chinese Academy of Sciences, Shanghai, 201210, China

^d Key Laboratory for Advanced Materials and Institute of Fine Chemicals, School of Chemistry and Molecular Engineering, East China University of Science and Technology, Shanghai, 200237, China

ARTICLE INFO

Keywords:
Photocatalyst
TiO₂ nanotubes
Carbon dots
H₂O₂ synthesis

ABSTRACT

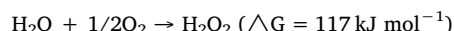
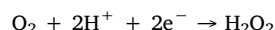
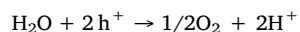
Photocatalytic synthesis of hydrogen peroxide (H₂O₂) from water and oxygen is an alternative route for clean energy storage and chemical synthesis, but still having problems with insufficient H₂O₂ productivity and solar-to-chemical energy conversion efficiency. Herein, we reported a hybrid catalyst of proton-form titania nanotube with carbon dot (HTNT-CD) that is highly efficient for the production of H₂O₂ under visible-light irradiation ($\lambda > 420$ nm, H₂O₂ productivity at 3.42 mmol g_{cat}⁻¹·h⁻¹), outperforming the titania catalysts containing noble metals and the carbon nitride catalysts reported previously. Multiple studies demonstrate that the protons on the HTNT-CD are crucial for the production of H₂O₂ by efficiently accelerating the half reaction of molecular oxygen reduction to form H₂O₂, and effectively hindering H₂O₂ decomposition under the irradiation conditions. This HTNT-CD catalyst gives solar-to-H₂O₂ apparent energy conversion efficiency at 5.2%, which is even 4.9 times of that (1.06%) over the catalyst derived from commercial P25 and CDs. More importantly, the HTNT-CD is stable, giving high H₂O₂ productivity in the continuous recycle tests.

1. Introduction

Hydrogen peroxide (H₂O₂) is regarded as a green oxidant that emits water as the sole by-product, which has been industrially used for disinfection, fine chemical synthesis, pollutant removal, and energy carrier for fuel cells [1–3]. In 2016, the global production of H₂O₂ was over 3 million metric tons, which is mainly manufactured from an-thraquinone method, involving multiple steps with production of environment unfriendly wastes and use of noble metals [4,5]. In contrast, the direct synthesis of H₂O₂ from gaseous hydrogen and oxygen over AuPd alloy or Pd nanoparticles has been extensively investigated [6–8], but this process requires a mixed gas of hydrogen and oxygen at high pressure [9]. Developing an alternative route to overcome these issues is still challenging.

Photocatalytic production of hydrogen peroxide on semiconductor, such as TiO₂, have been considered as a potentially promising route because of the significant advantages of employing water and molecular oxygen as the feedstocks [10–12]. Previous works have demonstrated

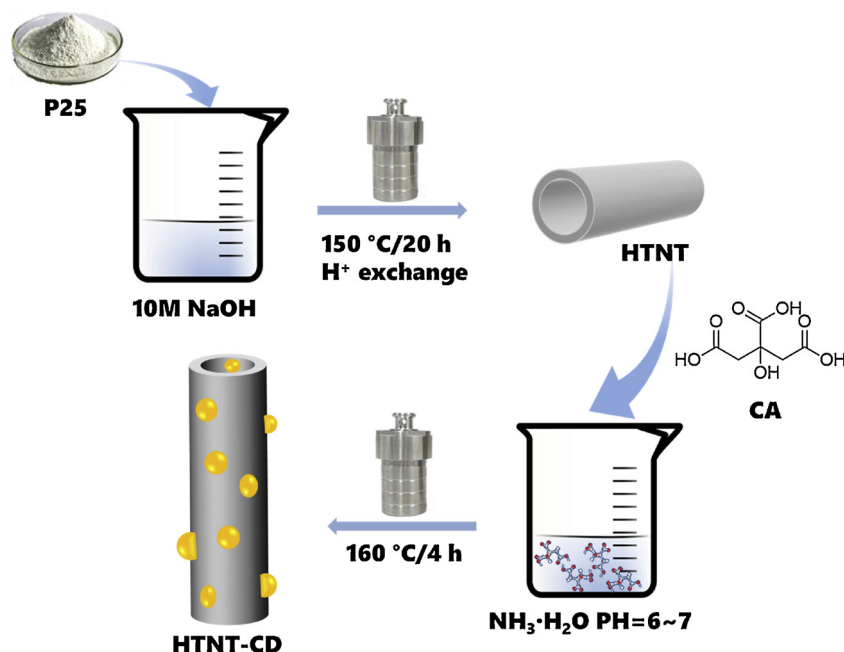
TiO₂-catalyzed H₂O₂ synthesis under UV irradiation, where the photoexcitation of the TiO₂ catalysts produces valence band holes (VB h⁺) oxidize water to produce O₂ and H⁺ [13–15]. Simultaneously, two-electron reduction of O₂ by the conduction band electrons (CB e⁻) displays dominant role for the production of H₂O₂. This process is thermodynamically unfavorable with ΔG at 117 kJ mol⁻¹ [14,15]. In addition, the one electron reduction of O₂ usually occurs as a dominant reaction to form superoxide radical, thus suppressing the two-electron reduction of O₂ to form H₂O₂ [16–18].



To overcome the aforementioned problems, the earlier successes were achieved in the noble metal loaded TiO₂, which gave significantly enhanced H₂O₂ productivity reaching as high as 2.08 mmol g_{cat}⁻¹ h⁻¹ under $\lambda > 300$ nm irradiation [19]. Further investigation using the

* Corresponding authors at: Key Lab of Biomass Chemical Engineering of Ministry of Education, College of Chemical and Biological Engineering, Zhejiang University, Hangzhou, 310027, China.

E-mail addresses: liangwang@zju.edu.cn (L. Wang), fsxiao@zju.edu.cn (F.-S. Xiao).



Scheme 1. Procedures for the synthesis of HTNT-CD. CA is citric acid.

diimide-modified graphitic carbon nitride ($\text{g-C}_3\text{N}_4$) exhibits the superior performances at $0.125 \text{ mmol g}_{\text{cat}}^{-1} \text{ h}^{-1}$ [14]. However, considering the vital role of H_2O_2 , enhancement of the photocatalyzed H_2O_2 productivity is necessary. Also, the H_2O_2 is unstable under the reaction conditions, which proceeded side reactions including decomposition into water and O_2 or oxidation of the alcohol sacrificial agent in the presence of TiO_2 , which are energy-favorable side reactions to decrease the H_2O_2 production [20–23]. With regard to the photocatalytic synthesis of H_2O_2 over titania based catalysts, potentially practical and sustainable routes need to employ noble-metal free catalysts and form H_2O_2 with high productivity, which is extremely difficult.

Herein, we report an efficient production of H_2O_2 over a titania-based catalyst without noble metals. Key to the success was the employment of carbon dots loaded acidic titania nanotubes (HTNT-CD), displaying H_2O_2 productivity at $3.42 \text{ mmol g}_{\text{cat}}^{-1} \text{ h}^{-1}$ under the visible-light irradiation ($\lambda > 420 \text{ nm}$), which readily outperforms the highly efficient carbon nitride catalysts and even the noble-metal loaded titania catalysts previously employed for the photocatalyzed H_2O_2 synthesis. Multiple characterization and catalytic investigation demonstrate the acidic sites on the HTNT-CD catalyst are crucial for the reactions, which accelerate the half reaction of molecular oxygen reduction to form H_2O_2 , and hinder the H_2O_2 decomposition under the irradiation conditions. This HTNT-CD catalyzed H_2O_2 production gives solar-to- H_2O_2 apparent energy conversion efficiency at 5.2%, which is even 4.9 times of that (1.06%) over the catalyst derived from commercial P25 and CD. More importantly, the HTNT-CD is stable and recycle, which is potentially important for practical applications.

2. Experimental

2.1. Materials

Citric acid monohydrate (CA), $\text{Ce}(\text{SO}_4)_2 \cdot 4\text{H}_2\text{O}$, Ferroin indicator solution ($\text{FeC}_{36}\text{H}_{24}\text{N}_6\text{SO}_4$), rhodamine B, HAuCl_4 , pyridine, and 2-PrOH were obtained from Aladdin Reagent Company. Absolute ethanol, hydrogen peroxide (H_2O_2 , 30 wt%), concentrated ammonia solution ($\text{NH}_3\text{H}_2\text{O}$, 28 wt%), concentrated hydrochloric acid (HCl), ferrous sulfate ($\text{Fe}(\text{SO}_4)_2 \cdot 7\text{H}_2\text{O}$), concentrated nitric acid (HNO_3), sodium hydroxide (NaOH), TiO_2 (P25), BaSO_4 , KBr, and AgNO_3 were purchased

from Real & lead Chemical Reagent Co. Ltd (Tianjin, China). All the reagents were of analytical pure grade without further purification.

2.2. Synthesis

2.2.1. Synthesis of H-form TiO_2 nanotubes (HTNT)

The TiO_2 nanotubes were synthesized via a hydrothermal method. As a typical run, 3 g of commercial P25 and 70 mL of NaOH aqueous solution (10 M) were mixed and stirred at room temperature for 20 min. Then the liquor was transferred into a 200 mL Teflon-lined stainless steel autoclave and heated at 150 °C for 20 h. After cooling down to room temperature, the white products were collected by centrifugation and washed with deionized water until the supernatant was neutral. After drying at 60 °C for 12 h, the Na-form TNT (NaTNT) was obtained. To acquire HTNT, the NaTNT sample was ion-exchanged with protons in an aqueous solution of HNO_3 (0.1 M). After filtrating, washing with water, and drying at 60 °C for 12 h under vacuum, the HTNT was finally obtained. After calcining HTNT at 400 °C for 2 h, the acidic sites were removed in the sample, giving titania nanotube sample (TNT).

2.2.2. Synthesis of HTNT-CD sample

As a typical run, 1.68 g of citric acid (0.2 M) was dissolved in 40 mL of deionized water. After stirring at room temperature for 1 h, the pH value of the solution was adjusted to 6.0 by adding $\text{NH}_3\text{H}_2\text{O}$. Then, 0.6 g of HTNT was dispersed into the solution under stirring for 10 min and ultrasonic treating for another 30 min. The mixture was transferred into a Teflon-lined stainless steel autoclave with 100 mL capacity and heated at 160 °C for 4 h. Finally, the product precipitates were obtained through filtrating, washing with deionized water, drying at 60 °C for 12 h under vacuum. The carbon dot loading was calculated to be 2.6 wt %. The synthesis procedures are shown in Scheme 1.

2.2.3. Synthesis of P25-CD, NaTNT-CD, and TNT-CD samples

These samples were synthesized from similar procedures to that of HTNT-CD, except using commercial P25, NaTNT, and TNT as carriers.

2.2.4. Synthesis of carbon dots (CDs)

As a typical run, 1.68 g of citric acid (0.2 M) was dissolved in 40 mL of deionized water. After stirring at room temperature for 1 h, the pH value of the solution was adjusted to 6.0 by adding $\text{NH}_3\text{H}_2\text{O}$. Then, the

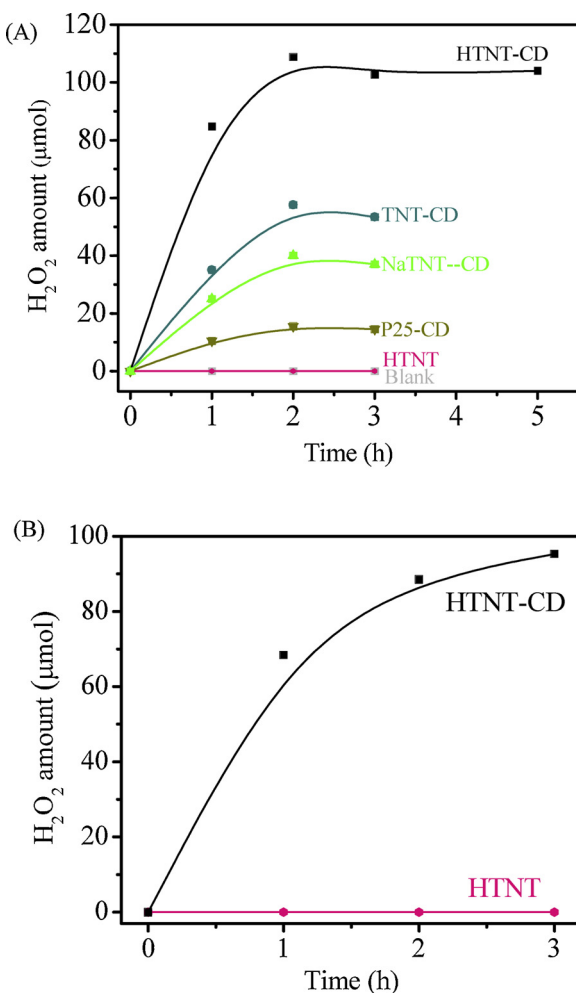


Fig. 1. Dependences H_2O_2 formation on time over various catalysts under (A) UV ($\lambda > 365 \text{ nm}$) and (B) visible light ($\lambda > 420 \text{ nm}$) irradiation. Reaction conditions: 20 mg of catalyst, 15 mL of water, 1 atm of air, and $28 \pm 1^\circ\text{C}$.

mixture was transferred into a Teflon-lined stainless steel autoclave with 100 mL capacity and heated at 160°C for 4 h. Finally, the obtained solution was filtered with a $0.22 \mu\text{m}$ porous membrane to remove the bulky carbon species and dialyzed for 2 days to remove the unreacted ions to obtain the CDs liquor.

The details in catalyst characterization are listed in Supplementary Information.

2.3. Photocatalytic H_2O_2 synthesis

The photocatalytic synthesis of H_2O_2 was performed in a 30 mL quartz reactor at 1 atm pressure. As a typical run, 20 mg of solid catalyst was dispersed in 15 mL of deionized water and stirred under dark for 1 h. This process benefits the dissolution of oxygen in water and full access to the catalyst surface before irradiation. Then, the liquor was localized under irradiation with a 350 W Xenon lamp under a constant stirring speed at 600 rpm. For the reactions under UV and visible light irradiation, the filters of $\lambda > 365$ and 420 nm were employed, respectively. The reaction temperature was controlled to be $28 \pm 1^\circ\text{C}$ by a circulatory water/ethanol bath during the reactions. After each reaction, the catalyst was separated by centrifugation. The amount of generated H_2O_2 was determined by a redox titration using standard $\text{Ce}(\text{SO}_4)_2 \cdot 4\text{H}_2\text{O}$ solution. The pure water was also titrated by the standard $\text{Ce}(\text{SO}_4)_2 \cdot 4\text{H}_2\text{O}$ solution, where the amount of $\text{Ce}(\text{SO}_4)_2 \cdot 4\text{H}_2\text{O}$ used in the solution was set as background. In the calculation of the H_2O_2 amount, the background of pure water was deducted. The titration was

carried out for over 5 times in each analysis, the error in the H_2O_2 amount analysis was $\pm 5\%$.

The photocatalytic decomposition of H_2O_2 was performed in a 30 mL quartz reactor at 1 atm N_2 . As a typical run, 15 mL of H_2O_2 solution (16 mM) was added into the reactor and cooled down to about 0°C in an ice bath. Then 20 mg of photocatalyst was added, the reactor was sealed and filled with nitrogen. The aforementioned procedures were performed under dark to minimize the H_2O_2 decomposition. Then the reactor was exposed to light irradiation with a 350 W Xenon lamp under a constant stirring. The amount of unreacted H_2O_2 was determined by a redox titration using standard $\text{Ce}(\text{SO}_4)_2 \cdot 4\text{H}_2\text{O}$ solution.

2.4. Solar energy apparent conversion efficiency measurement

The measurement of apparent quantum yield (AQY) was carried out in a quartz reactor. As a typical run, 15 mL of pure water and 20 mg of catalysts were added into the reactor. The AQY was measured under the controllable irradiation parameters including the intensity and the wavelength regions. The light source was CEL-HXF300 with a 300 W Xenon lamp equipped with monochromatic light filter at 365, 420, 450, 510, 550, and 600 nm, respectively (Beijing China Education Au-light Co., Ltd). The average intensities of irradiation to the reactor were determined by a spectroradiometer (PL-MW2000), which are measured to be 7.5, 43.4, 62.2, 59.4, 57.3, and 56.2 mW/cm^2 for wavelength at 365, 420, 450, 510, 550, and 600 nm, respectively. The irradiation for 60 min. The AQY was calculated using the following equation

$$\text{AQY} = \frac{N_e}{N_p} \times 100\% = \frac{N(\text{H}_2\text{O}_2) \times 2}{N(\text{photos})} \times 100\% = \frac{2 \times M \times N_A \times h \times c}{S \times P \times t \times \lambda} \times 100\%$$

The reaction electrons amount (N_e), incident photons (N_p), the amount of H_2O_2 molecules (M), the intensity of the irradiation (P), irradiation area (S), Avogadro constant (N_A), the speed of light (c), the wavelength of the monochromatic light (λ), the Planck constant (h), and the photoreaction time (t) are included in the equation [24–26].

2.5. Fenton reaction

After the photosynthesis of H_2O_2 with a 350 W Xenon lamp for 2 h (20 mg of catalyst, 15 mL of water, 1 atm of air, irradiation at $\lambda > 365 \text{ nm}$, $28 \pm 1^\circ\text{C}$), the solid catalyst was separated by filtration. Then 3 mL of liquor was added to a 1 mL of solution water containing rhodamine B (3 mg/L) and $\text{Fe}(\text{SO}_4)_2$. The changed concentration of rhodamine B was analyzed by UV-vis spectroscopy.

3. Results and discussion

3.1. Photocatalytic H_2O_2 synthesis

The as-prepared catalysts were evaluated in the photocatalytic synthesis of H_2O_2 in water under 1 atm of air at room temperature ($28 \pm 1^\circ\text{C}$). Fig. 1 shows the dependences of H_2O_2 amounts on time over various catalysts. Under irradiation simulating the sunlight frequencies ($\lambda > 365 \text{ nm}$), the blank run without catalysts was inactive for the reaction (Fig. 1A). Even when pure TiO_2 was added, the H_2O_2 was still undetectable. Interestingly, the CDs modified titania catalysts could efficiently catalyze the formation of H_2O_2 . For example, 84.7 μmol of H_2O_2 was formed over the HTNT-CD in a short reaction period of 1 h. Further prolonging the reaction time to 2 h gave 108.8 μmol of H_2O_2 , and then decreasing to 102.6–104 μmol for longer reaction (3–5 h, Fig. 1A). The decreased H_2O_2 amount was due to a slight decomposition of H_2O_2 under the reaction conditions. The kinetic study (Fig. 2) shows the H_2O_2 productivity over the HTNT-CD could reach $4.24 \text{ mmol g}_{\text{cat}}^{-1} \text{ h}^{-1}$, confirming the fast kinetic in the photocatalytic formation of H_2O_2 . In contrast, the Au supported on TiO_2 (Au/

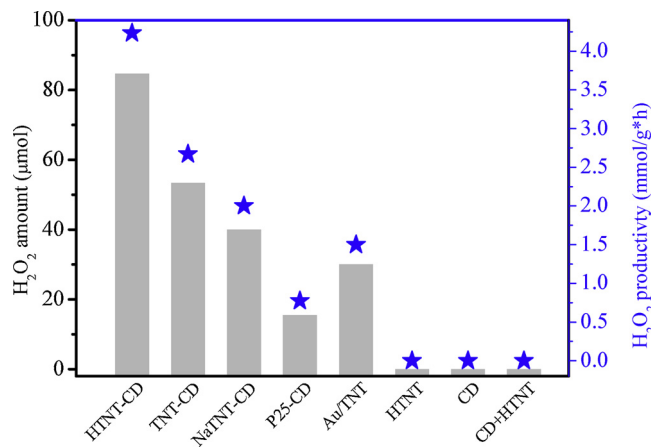


Fig. 2. The amount and productivity of synthesized H_2O_2 over various catalysts. Reaction conditions: 20 mg of catalyst, 15 mL of water, 1 atm of air, irradiation at $\lambda > 365 \text{ nm}$, $28 \pm 1 \text{ }^\circ\text{C}$, and reaction for 1 h.

TiO_2), which was regarded to be one of the fastest catalysts for photocatalytic synthesis of H_2O_2 [19], exhibited the H_2O_2 formation rate at $1.50 \text{ mmol g}_{\text{cat}}^{-1} \text{ h}^{-1}$. The loading amount of carbon dots on HTNT-CD was also optimized. Increase or decrease of carbon dot loadings (2.04 and 2.95 wt%) both reduced the H_2O_2 formation compared with the HTNT-CD containing carbon dot loading at 2.6 wt% (Fig. S1 and Table S1). In addition, the carbon dots supported on P25 (P25-CD) and NaTNT (NaTNT-CD) gave the amounts of H_2O_2 at 15.5 and 40.0 μmol after irradiation for 2 h (Figs. 1 and S2), respectively. All these data confirm the significant advance of the HTNT-CD beyond the other catalysts.

When the reaction was performed under visible light irradiation ($\lambda > 420 \text{ nm}$, Fig. 1B), the HTNT-CD catalyst still produced abundant H_2O_2 (95.3 μmol , reaction for 3 h). This result is even higher than the best result in literature achieved over diimide-modified graphitic carbon nitride ($\text{g-C}_3\text{N}_4$) with formed H_2O_2 amount at 50.6 μmol in long reaction time of 48 h, which has set a standard for photocatalytic synthesis of H_2O_2 [27]. A kinetic study revealed that the H_2O_2 production rate was $3.42 \text{ mmol g}_{\text{cat}}^{-1} \text{ h}^{-1}$, confirming the superior catalytic activity of the HTNT-CD under visible light irradiation. Figure S3 shows the amounts of generated H_2O_2 on the different wavelength with monochromatic filters over HTNT-CD catalyst. When the irradiation at 420, 450, 510, or 550 nm was employed, the H_2O_2 amount of 88.5, 68.7, 45.2, or 35.8 μmol was obtained, respectively.

In addition, we also explored the influence of oxygen concentration on reactivity. As shown in Fig. S4, the amount of produced H_2O_2 was significantly improved with increasing the oxygen concentrations from 3 to 50%, confirming that the abundant oxygen feeds could efficiently accelerate the synthesis of H_2O_2 . When the oxygen pressure exceeds 50%, the H_2O_2 amount did not change significantly. These results meant that when the oxygen concentration was over 50%, the performance of photocatalyst could be fully reached. However, considering the potential utilization of this process and sustainability of air as feedstock, the reactions were performed in 1 atm of air.

In order to evaluate the catalytic efficacy of various catalysts, we employed the apparent quantum yield (AQY) to estimate the catalytic efficacy under controllable irradiation. Table S2 presents the AQY values in the photo-catalyzed synthesis of H_2O_2 under UV and visible light irradiation over various photocatalysts. Under the UV irradiation ($\lambda = 365 \text{ nm}$), the AQY of HTNT-CD is 5.2%, which is significantly higher than that over NaTNT-CD (2.5%) and P25-CD (1.1%) catalysts. For the reaction under visible light irradiation ($\lambda = 420 \text{ nm}$), the HTNT-CD gives the AQY at 0.7%, which is still higher than that of NaTNT-CD (0.5%) and P25-CD (0.2%) catalyst. These data confirm a good efficacy of the HTNT-CD for solar energy conversion during the

photosynthesis of H_2O_2 . Figure S5 shows the correlation of the light absorbance spectra and AQY of several samples. The AQY values and the absorbance spectra are in good relationship with each other on the HTNT-CD and P25-CD samples, but the AQY values of HTNT-CD are always higher than those of P25-CD. Once exceeding the optical band gap, the apparent quantum efficiency of HTNT-CD rapidly drops from 0.7% at 420 nm to 0.01% at 590 nm.

More importantly, the HTNT-CD catalyst was reusable. After each reaction run, the catalyst can be easily separated from the reaction liquor by filtrating, washing and reused in the next run. The data characterizing the performances of the HTNT-CD in continuously recycle tests are presented in Fig. S6. Very interestingly, the amount of formed H_2O_2 was similar in the 2nd run (82 μmol). Further continuously recycle tests lead to a slightly decreased H_2O_2 amount in each run, which might be due to the leaching of carbon species on the HTNT-CD catalyst. Even if the 5th run, the H_2O_2 amount at 73 μmol was still achieved with a H_2O_2 productivity at $3.65 \text{ mmol g}_{\text{cat}}^{-1} \text{ h}^{-1}$, still outperforming the efficient catalysts reported in literatures (Table S3).

3.2. Structural characterization

All the results mentioned above confirm the outstanding performances of the HTNT-CD catalyst. Compared with conventional catalysts, the distinguishable efficacy in H_2O_2 production makes the HTNT-CD potentially useful for the solar-to-chemical energy conversion. In order to take a deep insight into the origin of the enhanced catalytic performances of the HTNT-CD, we performed multiple characterizations and catalytic investigations to study the relationship between catalyst structure and catalytic performances.

Fig. 3A gives XRD patterns of the HTNT-CD and HTNT samples, showing peaks at 24.8, 48.3, and 27.8°, which are assigned to the (101) and (200) diffractions of anatase, and (110) diffraction of rutile [28–31]. Compared with that of the P25, the peak of anatase (101) diffraction is extremely weak, and the peak at 75.1° of a typical anatase structure is absent on the XRD pattern of the HTNT-CD, which are typical features of low-dimensional TiO_2 materials with low crystallinity. Notably, the HTNT gives a peak at 9.3° assigned to the titanate species (Fig. S7), which benefits for the existence of abundant cations on the HTNT surface [32–34]. XRD patterns of other catalysts are shown in Fig. S8. N_2 sorption isotherms of the HTNT and HTNT-CD (Fig. 3B) exhibit typical type IV isotherms. An increased loop occurs in the curve at a relative pressure of $0.75 < P/P_0 < 0.95$, confirming the presence of abundant mesoporosity in both samples [35]. Correspondingly, the BET surface areas could be calculated as 310 m^2/g and 296 m^2/g over the HTNT and HTNT-CD samples, respectively. Similar textural parameters of HTNT and HTNT-CD demonstrate that the structure is well maintained during the loading of carbon dots. Their large surface areas reasonably benefit the access of substrate molecules to the surface of HTNT-CD during the photocatalytic reactions.

TEM characterization provides direct observation of the HTNT-CD sample. As shown in Fig. 4, the nanotubes with an internal diameter at 2.5–5.0 nm were observed. Interestingly, the wall thickness of the titania nanotubes was about 1.0–1.5 nm with several atomic layers (Figs. S9), which might explain the weak diffraction in the XRD patterns [36]. In addition, the walls with atomic-layer thickness are expected to facilitate the photogenerated charge separation. In the TEM images, the carbon dots with an average diameter at 2.3 nm are observed within and on the external surface of the HTNT, demonstrating the successfully loading carbon dots on the HTNT carrier via the hydrothermal synthesis. Importantly, the morphology of the HTNT and thickness of the nanotube walls were unchanged before and after loading the CDs (Figs. 4 and S9B), confirming the high stability of the HTNT under the hydrothermal process. As well, the P25-CD catalyst was characterized by the TEM characterization to observe the CDs supported on P25 crystals, giving the average diameter of CDs was at 2.5 nm, which is similar to that of the HTNT-CD sample (Figs. S10 and S11).

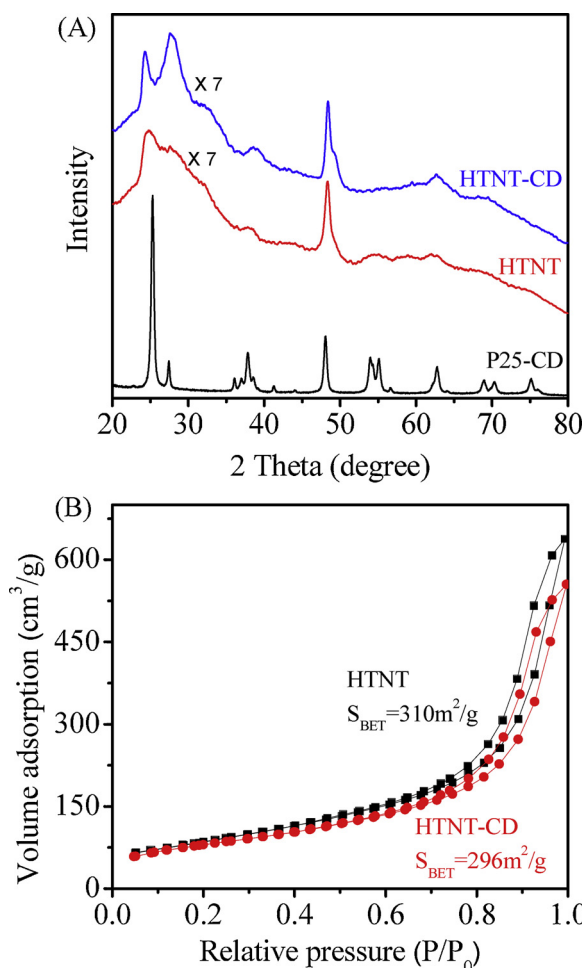


Fig. 3. (A) XRD patterns of HTNT, HTNT-CD, and P25-CD samples and (B) N₂ sorption isotherms of HTNT and HTNT-CD samples.

Fig. 5 shows Raman spectra of various samples. The P25 and P25-CD samples give typical Raman bands at 144 (E_g), 197 (E_g), 399 (B_{1g}), 513 (A_{1g}), 519 (B_{1g}), and 639 cm⁻¹ (E_g), which are assigned to the

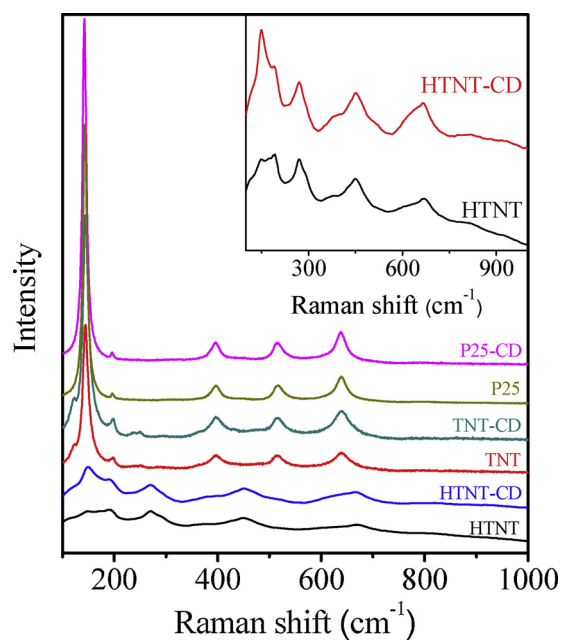


Fig. 5. Raman spectra of various samples. Inset: enlarged view of the spectra of the HTNT and HTNT-CD samples.

modes of typical TiO₂ [37]. Compared with P25-based samples, the HTNT and HTNT-CD exhibit much weak and broad bands, because of the low crystallinity of HTNT with thin walls. Notably, the HTNT and HTNT-CD have the E_{1g} modes at 148 cm⁻¹, exhibiting a blue shift of 4 cm⁻¹ compared with that of P25 (144 cm⁻¹). This blue shift is reasonable due to atomic thickness of HTNT walls, which changes the symmetry of Ti-O-Ti species on the surface and subsurface of the HTNT [38]. Interestingly, compared with the Raman spectrum of P25 sample, the HTNT has an additional band at 270 cm⁻¹ associated with the Ti-O-H species from proton exchange with HNO₃, which might provide Brønsted acid sites on the HTNT surface. The mode at 270 cm⁻¹ is well maintained after loading CDs on the HTNT. However, after calcination of the HTNT at 400 °C, the mode of Ti-O-H species is almost undetectable on the TNT sample due to the condensation of Ti-OH to form Ti-O-Ti, giving improved crystallinity on TNT compared with

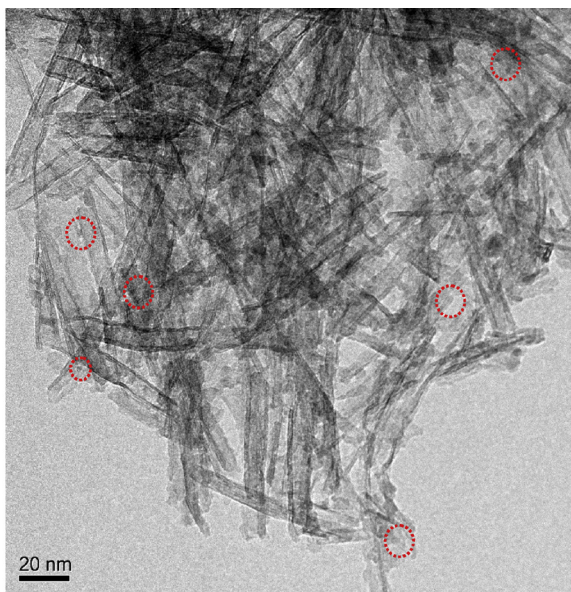
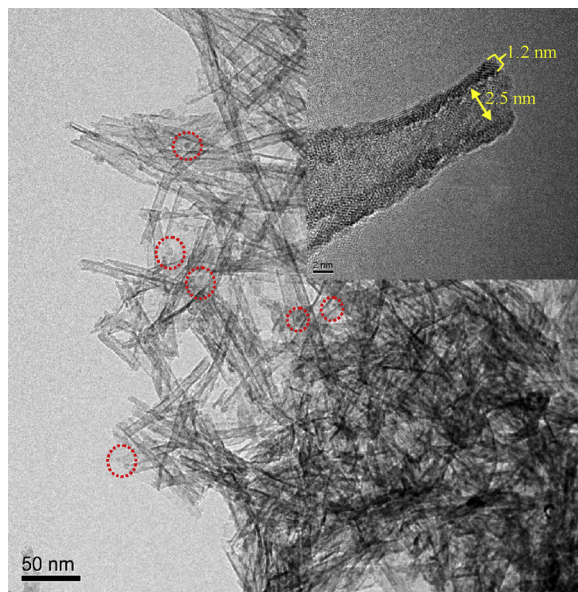


Fig. 4. TEM images of HTNT-CD sample. The red cycles highlighted the CDs. Inset: enlarged view of the sample with scale bar at 2 nm (For interpretation of the references to colour in this figure legend, the reader is referred to the web version of this article).

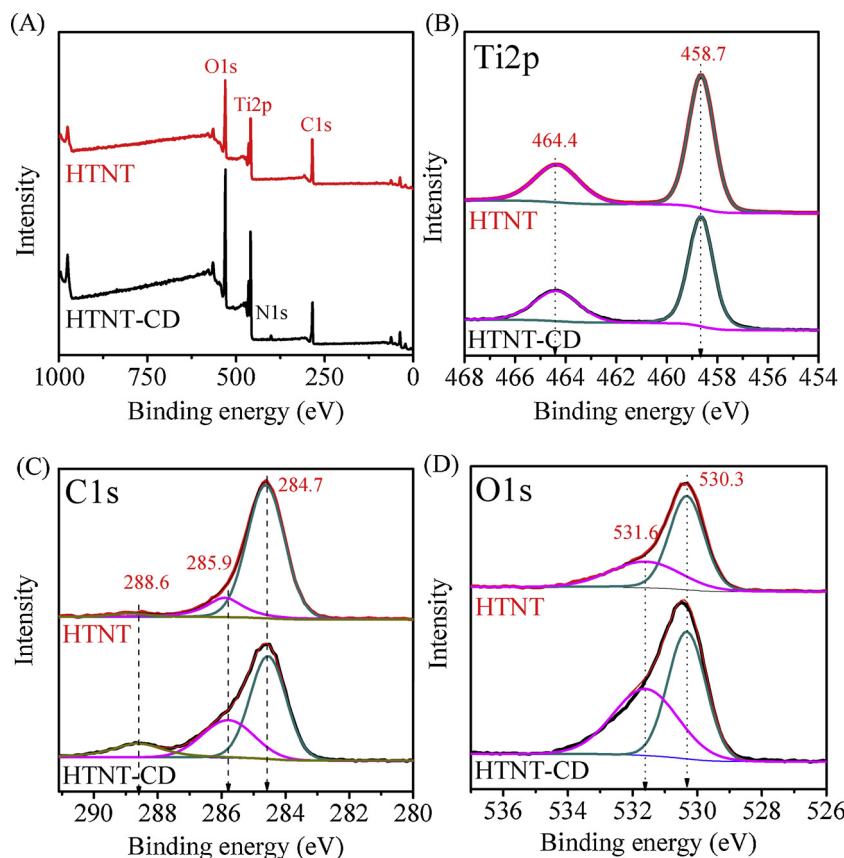


Fig. 6. (A) Survey, (B) Ti2p, (C) O1s, and (D) C1s XPS spectra of the HTNT and HTNT-CD samples.

HTNT [32,39–41].

XPS spectra of the HTNT and HTNT-CD samples are given in Fig. 6. Both samples exhibit similar Ti2p XPS spectra, assigning to typical Ti^{4+} species (Fig. 6B). In the C1s XPS spectra, the HTNT and HTNT-CD give typical peaks at 284.7, 285.9, and 288.6 eV (Fig. 6C), which are assigned to the background carbon, C–O, and C=O species [42–44]. The remarkably enhanced C1s signals of C–O and C=O on HTNT-CD compared with HTNT is reasonably assigned to the existence of CDs. In the O1s XPS spectra, the HTNT-CD and HTNT samples exhibit the peaks at 530.3 and 531.6 eV. The peak at 530.3 eV is assigned to the lattice oxygen, and the peak at 531.6 eV is from the combined contribution of Ti–OH group and C=O in the carbon dots [45–47]. The much stronger O1s band at 531.6 eV over HTNT-CD than HTNT might be due to the loading of carbon dots. The successful formation of CDs on the HTNT-CD, TNT-CD, and P25-CD samples is further evidenced by FTIR spectroscopy (Fig. S12), which exhibit the bands at 3130–3140, 1620–1644, and 1400 cm^{-1} , assigning to the N–H, C–N, and C=C bonds, respectively [48–50]. These results are in good agreement with those on the XPS characterization.

Fig. 7A shows UV-vis spectra of various titania-based samples. The P25 exhibits adsorption bands only in the UV region with a threshold at 387 nm and band-gap energy at *ca.* 3.20 eV [51]. Interestingly, the HTNT gives a threshold at 394 nm with a band-gap energy at *ca.* 3.15 eV, which attributed to the atomic layer thickness of the HTNT with abundant surface/sub-surface defects to shift the valence band and narrow the band-gap. Furthermore, when the carbon dots were loaded on the P25 and HTNT, the samples exhibit obvious adsorption band in visible region with thresholds at 430 and 415 nm over P25-CD and HTNT-CD, respectively. These features are possible to carry out the reaction under visible light irradiation, which are in good agreement with the results in previous literature that the combination of TiO_2 with carbon materials enables to extend the photoresponse into visible-light

range [51–53].

The role of CDs modification to the catalysts was further presented by the surface photovoltage (SPV) measurements, which is powerful technique to characterize the efficiency of the charge separation [54]. As shown in Fig. S13, these samples exhibit obvious SPV under radiation, originated from the separation of photogenerated electron and hole. Particularly, the CDs modified samples of P25-CD and HTNT-CD exhibited significantly enhanced SPV than the corresponding CDs-free P25 or HTNT samples, confirming the positive role of CDs modification for enhancing the separation of photogenerated electrons and holes. Particularly, the HTNT-CD gives the highest SPV among these samples, owing to the high surface area and atomic-thickness wall, which facilitate the formation of nanostructure with abundant TiO_2 -CD heterojunctions.

Additional evidences were obtained *via* the room temperature photoluminescence (PL) spectra (Fig. 7B), where all the samples exhibited broad signals at *ca.* 468 nm, originated from the irradiative recombination of free electrons in shallow raps below conductive band and free holes at the valence band edge. The HTNT and TNT both exhibited broad signal at *ca.* 468 nm with similar intensity in the PL spectra, which indicate similar electron-hole separation on the two samples although the two samples have significantly different crystallinities. Interestingly, it is worth mentioning that the TNT and HTNT have enhanced electron-hole separation compared with P25, as confirmed by weaker PL intensities of TNT and HTNT samples. Considering that the TNT, HTNT, and P25 are all titania-based materials, the enhanced charge separation should be reasonably assigned to the thin walls of nanotube structure with abundant defects [55–58]. After loading the carbon species, the HTNT-CD has a much weaker signal than the other samples, indicating that the HTNT-CD can effectively suppress the electron-hole recombination [59,60]. These results are well consistent with those from the SPV measurement.

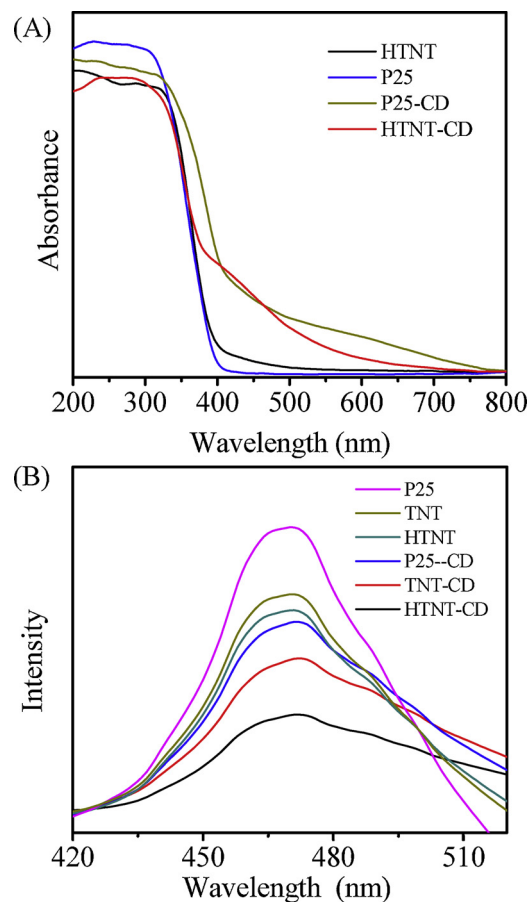


Fig. 7. (A) UV-vis and (B) PL spectra of various samples.

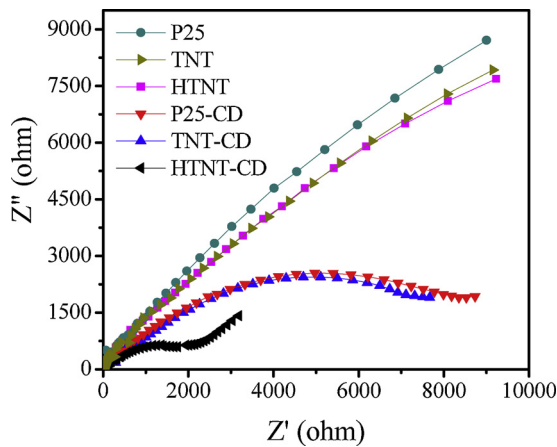


Fig. 8. EIS curves of various samples.

Electrochemical impedance spectroscopy (EIS) was performed to understand the electrical conductivity of the samples before and after CDs loading. The titania samples without CDs (P25, HTNT, and TNT) display a big arc radius (Fig. 8), suggesting the high charge transfer resistance. However, it is reasonable that the HTNT exhibits higher conductivity than P25 even if the former has lower crystallinity. This reason is assigned to the presence of protons and titanate species in the HTNT sample. After loading the CDs, the arc radius is remarkably decreased over HTNT-CD, TNT-CD, and P25-CD, suggesting the enhanced charge transfer efficacy. Among these samples, the HTNT-CD exhibits the best charge transfer efficacy, which benefits the electron-hole separation during the photocatalysis. This feature is reasonably assigned

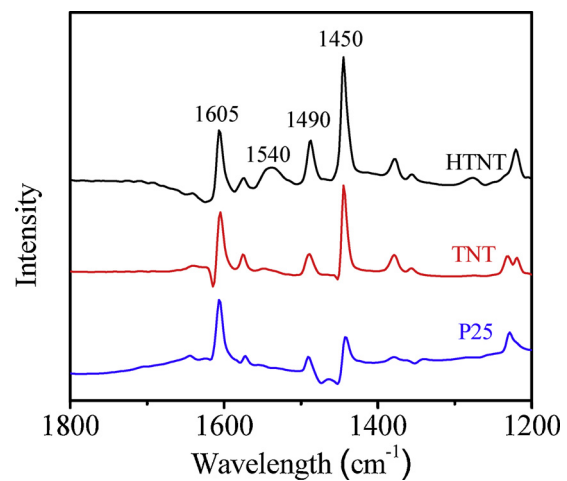


Fig. 9. Pyridine-adsorption FTIR spectra of the HTNT, TNT, and P25 samples.

to the protons on the samples, which efficiently accelerate the activity in photoreduction [61,62], in good agreement with those from SPV measurements and PL spectra.

3.3. Role of acidity

The pyridine-adsorption FTIR spectroscopy was performed to understand the acidity of the P25, TNT, and HTNT samples. As shown in Fig. 9, the samples give strong bands at 1605, 1540, 1490, and 1450 cm⁻¹. The bands at 1450 and 1605 cm⁻¹, which are assigned to the pyridine coordinatively bonded on Lewis acid sites [63], exist on all the P25, TNT, and HTNT samples. Compared with P25 and TNT, the spectrum of HTNT gives an additional band at 1540 cm⁻¹ assigned to the pyridine bonded to the Brønsted acid sites [60,64]. This feature should be reasonably attributed to the titanate species on the catalyst surface, which forms abundant protons on the catalyst by the ion-exchange treatment in the synthesis of HTNT [65], as confirmed by the Ti-O-H band in the Raman spectrum. These results indicate that P25 and TNT have only Lewis acid sites, which are in good agreement with the features of general titania, while HTNT has both Lewis and Brønsted acid sites.

Many reaction mechanism has been reported in the literature [1,47,53,66–68]. In order to take insight into the roles of electrons and holes for the H₂O₂ synthesis, the reactions were carried out with the presence of various radical scavengers. Fig. 10 shows the data

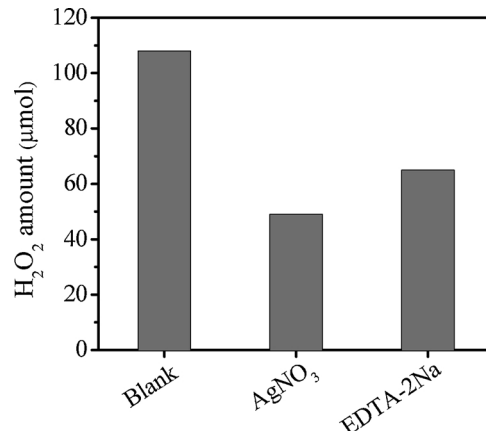


Fig. 10. The produced amounts of H₂O₂ over HTNT-CD catalyst with different additives. Reaction condition: 20 mg of HTNT-CD catalyst, 15 mL of water, 1 atm of air, different additives, 2 h, and 28 ± 1 °C. Blank is the reaction without additives.

characterizing the produced amounts of H_2O_2 with different additives of AgNO_3 and EDTA-2Na. In these cases, the H_2O_2 are still produced but the amounts are remarkably lower than those in the additive-free reaction (blank run in Fig. 10). For example, when AgNO_3 was added as an electron trapping agent [69] in the system, the amount of H_2O_2 was 49 μmol . When EDTA-2Na was added as a hole trapping agent in the system [69], the amount of H_2O_2 was 65 μmol . These results demonstrate that both the electrons and holes participate in the H_2O_2 production.

On the basis of these results and the mechanism reported in the literature [46,70], we proposed that the H_2O_2 were formed by two pathways, including (i) $\text{O}_2 + 2\text{H}^+ + 2\text{e}^- \rightarrow \text{H}_2\text{O}_2$ pathway on the photo-generated electrons and (ii) $\text{h}^+ + \text{H}_2\text{O} \leftrightarrow \text{H}^+ + \cdot\text{OH} + \cdot\text{OH} \leftrightarrow \text{H}_2\text{O}_2$ pathway on photo-generated holes, where the mechanism (ii) does not require molecular oxygen while the mechanism (i) really requires the presence of oxygen. In the mechanism (i), the protons are favorable for the coupled electron transfer (PCET) [13,27]. Therefore, the existence of oxygen indeed effectively enhanced the H_2O_2 production [71–75].

To further understand the acidic influence for H_2O_2 production, we performed the half reaction of water oxidation with AgNO_3 as a sacrificial electron acceptor to produce oxygen, and O_2 reduction with 2-PrOH as a sacrificial electron donor to produce H_2O_2 on the HTNT-CD and P25-CD catalysts. In these reactions with sacrificial substrate molecules under irradiation at $\lambda > 365 \text{ nm}$, the HTNT-CD exhibited a slightly higher amount of oxygen than P25-CD in the water oxidation (Fig. 11A). However, in the half reaction of H_2O_2 synthesis, the HTNT-CD exhibited two-fold higher H_2O_2 amount than the P25-CD. Similar phenomena were also observed in the equivalent tests under visible irradiation ($\lambda > 420 \text{ nm}$, Fig. S14). We concluded that the enhanced performance of HTNT-CD is due to the acidity, the abundant protons close to the catalyst surface shifted the reaction balances to H_2O_2 formation in $\text{O}_2 + 2\text{H}^+ + 2\text{e}^- = \text{H}_2\text{O}_2$. Compared with the reported reaction system employing liquid acids for corrosivity and waste water production [71,76–83], the HTNT-CD catalyst as solid acid has remarkably advantage in the environmental concerns.

In addition, the H_2O_2 decomposition under reaction conditions also reduced the productivity. Actually, the addition of acids to the reaction medium has been extensively studied as a means of stabilizing the synthesized H_2O_2 . Decreasing the pH of the reaction by addition of nitric, sulfuric, phosphoric, and hydrochloric acids has shown to be essential in achieving high yields of H_2O_2 under various reaction conditions [8,76–84]. Therefore, we investigated the stability of H_2O_2 in the reaction liquor under irradiation. As shown in Fig. 12A, the H_2O_2 was decomposed slowly in water without catalysts, reaching 75.1% (C/C_0) of the original concentration after irradiation for 4 h. When the titania-based catalysts were present in the liquor, the H_2O_2 decomposition was remarkably enhanced. For example, the H_2O_2 was nearly undetectable in the liquor over the P25-CD, and the H_2O_2 concentration was only 12.5% of the original value over the TNT-CD. Interestingly, the H_2O_2 decomposition was extensively hindered over the acidic catalysts of HTNT and HTNT-CD, giving the C/C_0 values at 51 and 42%, respectively. These data confirm that the HTNT and HTNT-CD could efficiently stabilize the H_2O_2 under the reaction conditions. Considering that the most significant difference between HTNT-CD and other catalysts are the Brønsted acidity, the stability effect of HTNT-CD for H_2O_2 should be reasonably assigned to the acidity rather than other factors. This phenomenon was further confirmed by the H_2O_2 decomposition tests with additional liquid acids, where the added hydrochloric acid effectively hinders the H_2O_2 decomposition (Fig. 12B).

3.4. Utilization of the photo-synthesized H_2O_2

In order to expand the significance of our experiments, we designed a subsequent fenton reaction to degrade rhodamine B using the photo-synthesized H_2O_2 [85,86]. After the reaction over HTNT-CD, the

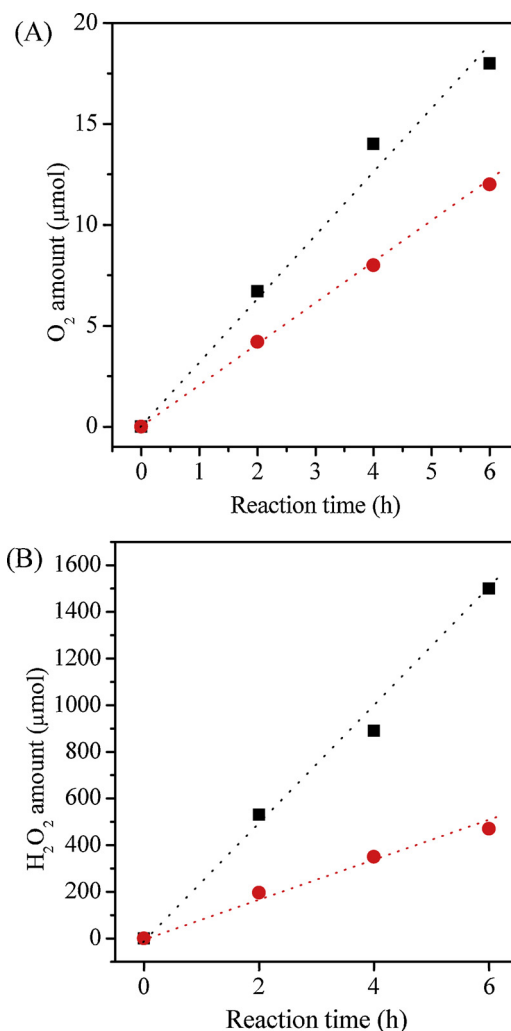


Fig. 11. Dependences of product amounts on time over the HTNT-CD and P25-CD in half reactions under irradiation $\lambda > 365 \text{ nm}$ including (A) formation of O_2 in AgNO_3 aqueous solution under 1 atm of Ar and (B) formation of H_2O_2 in 2-PrOH aqueous solution under 1 atm of O_2 .

photocatalyst was filtered to get the liquor containing H_2O_2 , which is subsequently used for the degradation of rhodamine B with the existence of FeSO_4 (Scheme 2). Interestingly, the rhodamine B was efficiently degraded as confirmed by the UV-vis characterization and color change observation (Fig. 13). However, when the equivalent experiment was performed using photo-synthesized H_2O_2 over P25-CD catalyst, the efficacy for rhodamine B degradation was relatively poor, which is reasonable because of the insufficient amount of H_2O_2 in the liquor. Considering that the fenton process has been already widely utilized for waste-water treatment, the aforementioned process makes the HTNT-CD catalyzed photo-synthesis of H_2O_2 potentially valuable for practical applications.

4. Conclusion

In summary, we developed an efficient photocatalyst of HTNT-CD for the efficient synthesis of H_2O_2 from water and oxygen. The HTNT-CD gives high H_2O_2 productivity at $3.42 \text{ mmol g}_{\text{cat}}^{-1} \text{ h}^{-1}$, outperforming the titania catalysts containing noble metals and the *state-of-the-art* carbon nitride catalysts. Key to the success is the acidic protons on the surface of HTNT-CD catalyst, which remarkably accelerates the half reaction of oxygen reduction with electrons to form H_2O_2 , as well as stabilizes H_2O_2 under the reaction conditions to hinder the H_2O_2

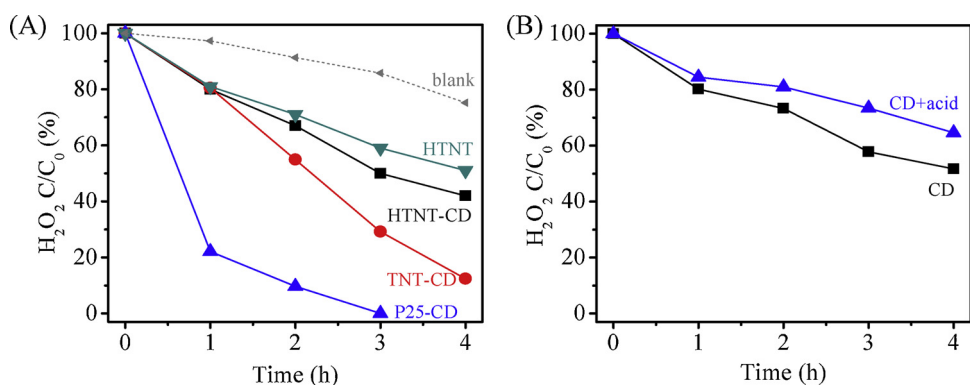
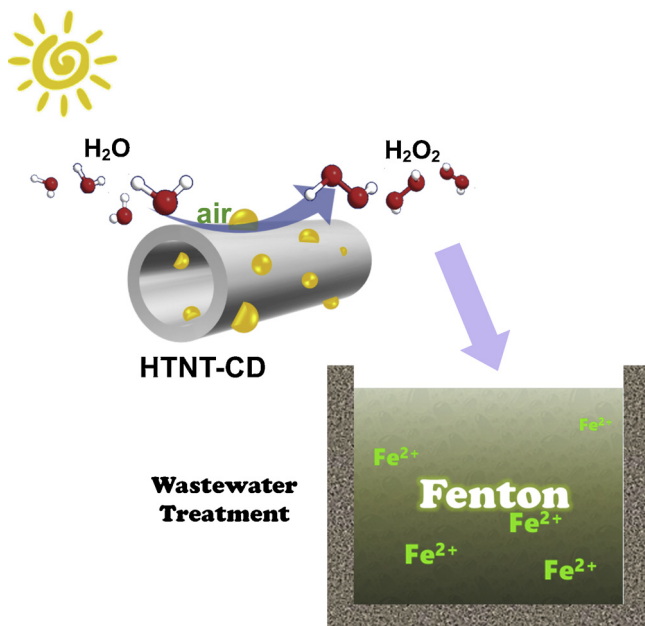


Fig. 12. The photocatalytic decomposition of H_2O_2 ($\text{C}_0 = 16 \text{ mM}$) over various catalysts. Catalyst amount at 1.33 g/L photocatalyst, room temperature, and 1 atm of N_2 , and UV-vis irradiation $\lambda > 365 \text{ nm}$.



Scheme 2. Photocatalytic synthesis of H_2O_2 , followed by using the H_2O_2 in the Fenton reaction for wastewater treatment.

decomposition. This HTNT-CD catalyzed H_2O_2 production with solar-to- H_2O_2 energy transformation efficiency at 5.2%, which is even 4.9 times of that (1.06%) over the catalyst derived from commercial P25 and CDs. It is believed the strategy employing solid acids might open a way for developing more efficient catalysts for solar energy conversion and H_2O_2 synthesis in the future.

Acknowledgments

This work is supported by the National Key Research and Development Program of China (2018YFB0604801), National Natural Science Foundation of China (21822203, 91645105, and 91634201), Natural Science Foundation of Zhejiang Province (LR18B030002), and Foundation of Key Laboratory of Low-Carbon Conversion Science & Engineering, Shanghai Advanced Research Institute, Chinese Academy of Sciences (KLLCCSE-201605).

Appendix A. Supplementary data

Supplementary material related to this article can be found, in the online version, at doi:<https://doi.org/10.1016/j.apcatb.2018.11.087>.

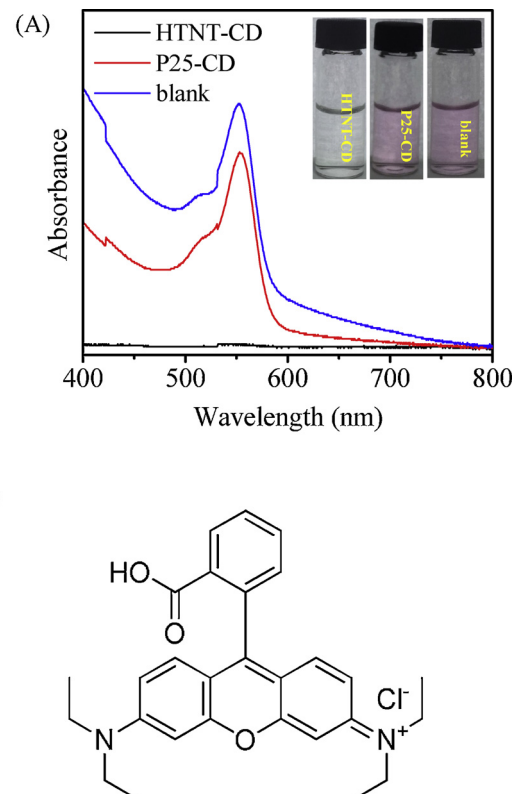


Fig. 13. (A) UV-vis spectra of the liquor after fenton degradation of Rhodamine B using different H_2O_2 sources from the photosynthesis over HTNT-CD and P25-CD catalysts. Inset: the photographs of the liquors. (B) Rhodamine B molecule.

References

- [1] K. Mase, M. Yoneda, Y. Yamada, S. Fukuzumi, *Nat. Commun.* 7 (2016) 11470.
- [2] R.S. Disselkamp, *Energy Fuels* 22 (2008) 2771–2774.
- [3] A.E. Sanli, A. Aytac, *Int. J. Hydrogen Energy* 36 (2011) 869–875.
- [4] J.M. Campos-Martin, G. Blanco-Brieva, J.L.G. Fierro, *Angew. Chem. Int. Ed.* 45 (2006) 6962–6984.
- [5] D. Hancu, H. Green, E.J. Beckman, *Ind. Eng. Chem. Res.* 41 (2002) 4466–4474.
- [6] V.R. Choudhary, A.G. Gaikwad, S.D. Sansare, *Angew. Chem. Int. Ed.* 40 (2001) 1776–1779.
- [7] M. Piccinini, E. Ntaijua, J.K. Edwards, A.F. Carley, J.A. Moulijn, G.J. Hutchings, *Phys. Chem. Chem. Phys.* 12 (2010) 2488–2492.
- [8] J.K. Edwards, B. Solsona, E. Ntaijua, A.F. Carley, A.A. Herzing, C.J. Kiely, G.J. Hutchings, *Science* 323 (2009) 1037–1041.
- [9] D. Hancu, H. Green, E.J. Beckman, *Ind. Eng. Chem. Res.* 41 (2002) 4466–4474.
- [10] C. Kormann, D. Bahnemann, M.R. Hoffmann, *Environ. Sci. Technol.* 22 (1988) 798–806.
- [11] X. Wang, K. Maeda, A. Thomas, K. Takanabe, G. Xin, J.M. Carlsson, K. Domen, M. Antonietti, *Nat. Mater.* 8 (2009) 76–80.

[12] S.J. Kim, G.-H. Moon, H.J. Kim, Y.D. Mun, P. Zhang, J.W. Lee, W.Y. Choi, *Appl. Catal. B* 357 (2018) 51–58.

[13] Y. Kofuji, Y. Isobe, Y. Shiraishi, H. Sakamoto, S. Tanaka, S. Ichikawa, T. Hirai, *J. Am. Chem. Soc.* 138 (2016) 10019–10025.

[14] Y. Shiraishi, S. Kanazawa, Y. Sugano, D. Tsukamoto, H. Sakamoto, S. Ichikawa, T. Hirai, *ACS Catal.* 4 (2014) 774–780.

[15] Y. Kofuji, S. Ohkita, Y. Shiraishi, H. Sakamoto, S. Tanaka, S. Ichikawa, T. Hirai, *ACS Catal.* 6 (2016) 7021–7029.

[16] X. Li, C. Chen, J. Zhao, *Langmuir* 17 (2001) 4118–4122.

[17] V. Maurino, C. Minero, G. Mariella, E. Pelizzetti, *Chem. Commun. (Camb.)* 36 (2005) 2627–2629.

[18] K.A. Kurak, A.B. Anderson, *J. Phys. Chem. C* 113 (2009) 6730–6734.

[19] M. Teranishi, S.-I. Naya, H. Tada, *J. Am. Chem. Soc.* 132 (2010) 7850–7851.

[20] Y. Shiraishi, S. Kanazawa, D. Tsukamoto, A. Shiro, Y. Sugano, T. Hirai, *ACS Catal.* 3 (2013) 2222–2227.

[21] M.A. Henderson, *Surf. Sci. Rep.* 66 (2011) 185–297.

[22] S. Goldstein, D. Aschengrau, Y. Diamant, J. Rabani, *Environ. Sci. Technol.* 41 (2007) 7486–7490.

[23] G.-H. Moon, W. Kim, A.D. Bokare, N.-E. Sung, W. Choi, *Energy Environ. Sci.* 7 (2014) 4023–4028.

[24] W.J. Jiang, Q.S. Ruan, J.J. Xie, X.J. Chen, Y.F. Zhu, J.W. Tang, *Appl. Catal. B* 236 (2018) 428–435.

[25] H.H. Ou, P.J. Yang, L.H. Lin, M. Anpo, X.C. Wang, *Angew. Chem. Int. Ed.* 56 (2017) 10905–10910.

[26] Y.X. Li, S.X. Ouyang, H. Xu, X. Wang, Y.P. Bi, Y.F. Zhang, J.H. Ye, *J. Am. Chem. Soc.* 138 (2016) 13289–13297.

[27] Y. Shiraishi, S. Kanazawa, Y. Kofuji, H. Sakamoto, S. Ichikawa, S. Tanaka, T. Hirai, *Angew. Chem. Int. Ed.* 53 (2014) 13454–13459.

[28] M. Zhang, W. Jiang, D. Liu, J. Wang, Y. Liu, Y. Zhu, *Appl. Catal. B* 183 (2016) 263–268.

[29] H. Yamashita, Y. Ichihashi, M. Harada, G. Stewart, M.A. Fox, M. Anpo, *J. Catal.* 158 (1996) 97–101.

[30] H. Zhang, X.J. Lv, Y.M. Li, Y. Wang, J.H. Li, *ACS Nano* 4 (2010) 380–386.

[31] C.H. Li, C. Koenigsmann, W.D. Ding, B. Rudshteyn, K.R. Yang, K.P. Regan, S.J. Konezny, V.S. Batista, G.W. Brudvig, C.A. Schmuttenmaer, J.-H. Kim, *J. Am. Chem. Soc.* 137 (2015) 1520–1529.

[32] X.M. Sun, Y.D. Li, *Chem. Eur. J.* 9 (2003) 2229–2289.

[33] Z.R. Tian, J.A. Voigt, J. Lin, B. Mckenzie, H. Xu, *J. Am. Chem. Soc.* 82 (2003) 281.

[34] T. Kubo, A. Nakahira, *J. Phys. Chem. C* 112 (2008) 1658–1662.

[35] R.Y. Ma, L. Wang, S. Wang, C.T. Wang, F.-S. Xiao, *Appl. Catal. B* 212 (2017) 193–200.

[36] L. Zhang, S.Z. Qiao, Y.G. Jin, H.G. Yang, S. Budihartono, F. Stahr, Z.F. Yan, X.L. Wang, Z.P. Hao, G.Q. Lu, *Adv. Funct. Mater.* 18 (2008) 3203–3212.

[37] C. Ratanatwanate, C.R. Xiong, K.J.B. Jr, *ACS Nano* 2 (2008) 1682–1688.

[38] L. Qian, Z.-L. Du, S.-Y. Yang, Z.-S. Jin, *J. Mol. Struct.* 749 (2005) 103–107.

[39] M. Nischk, P. Mazierski, M. Gazda, A. Zaleska, *Appl. Catal. B* 144 (2014) 674–685.

[40] D.V. Bavykin, J.M. Friedrich, F.C. Walsh, *Adv. Mater.* 18 (2006) 2807–2824.

[41] M. Kitano, E. Wada, K. Nakajima, S. Hayashi, S. Miyazaki, H. Kobayashi, M. Hara, *Chem. Mater.* 25 (2013) 385–393.

[42] Y. Cong, X. Li, Y. Qin, Z. Dong, G. Yuan, Z. Cui, X. Lai, *Appl. Catal. B* 107 (2011) 128–134.

[43] Q. Xiang, K. Lv, J. Yu, *Appl. Catal. B* 96 (2010) 557–564.

[44] S.D. Perera, R.G. Mariano, K. Vu, N. Nour, O. Seitz, Y. Chabal, K.J. Balkus Jr., *ACS Catal.* 2 (2012) 949–956.

[45] X.J. Yu, J.J. Liu, Y.C. Yu, S.L. Zuo, B.S. Li, *Carbon* 68 (2014) 718–724.

[46] Y.R. Li, Z.M. Liu, Y.C. Wu, J.T. Chen, J.Y. Zhao, F.M. Jin, P. Na, *Appl. Catal. B* 224 (2018) 508–517.

[47] X.X. Zou, J.K. Liu, J. Su, F. Zuo, J.S. Chen, P.Y. Feng, *Chem. Eur. J.* 19 (2013) 2866–2873.

[48] N.C.T. Martins, J. Ângelo, A.V. Girão, T. Trindade, L. Andrade, A. Mendes, *Appl. Catal. B* 193 (2016) 67–74.

[49] J. Yu, Y. Su, B. Cheng, M. Zhou, *J. Mol. Catal. A Chem.* 258 (2006) 104–112.

[50] J.C. Liu, N. Wang, Y. Yu, Y. Yan, H.Y. Zhang, J.Y. Li, J.H. Yu, *Sci. Adv.* 3 (2017) e1603171.

[51] S. Bai, L. Yang, C.L. Wang, Y. Lin, J.L. Lu, J. Jiang, Y.J. Xiong, *Angew. Chem. Int. Ed.* 54 (2015) 14810–14814.

[52] C.B. Zhang, F.D. Liu, Y.P. Zhai, H. Ariga, N. Yi, Y.C. Liu, A. Kiyotaka, F.-S. Maria, H. He, *Angew. Chem. Int. Ed.* 51 (2012) 9628–9632.

[53] N. Zhang, S.Q. Liu, X.Z. Fu, Y.-J. Xu, *J. Phys. Chem. C* 115 (2011) 9136–9145.

[54] Q. Xiang, J. Yu, M. Jaroniec, *Nanoscale* 3 (2011) 3670–3678.

[55] Y.B. He, A. Tilocca, O. Dulub, A. Selloni, U. Diebold, *Nat. Mater.* 8 (2009) 585–589.

[56] J. Lee, D.C. Sorescu, X.Y. Deng, *J. Am. Chem. Soc.* 133 (2011) 10066–10069.

[57] E. Lira, S. Wendt, P.P. Huo, J.Ø. Hansen, R. Streber, S. Porsgaard, Y.Y. Wei, R. Bechstein, E. Lægsgaard, F. Besenbacher, *J. Am. Chem. Soc.* 133 (2011) 6529–6532.

[58] J.Q. Yan, G.J. Wu, N.J. Guan, L.D. Li, Z.X. Li, X.Z. Cao, *Phys. Chem. Chem. Phys.* 15 (2013) 10978–10988.

[59] Y.Y. Wang, W.J. Yang, X.J. Chen, J. Wang, Y.F. Zhu, *Appl. Catal. B* 220 (2018) 337–347.

[60] R.Y. Ma, L. Wang, B.S. Zhang, X.F. Yi, A.M. Zheng, F. Deng, X.H. Yan, S.X. Pan, X. Wei, K.-X. Wang, D.S. Su, F.-S. Xiao, *ChemSusChem* 9 (2016) 2759–2764.

[61] Y. Zhang, W.Q. Cui, W.J. An, L. Liu, Y.H. Liang, Y.F. Zhu, *Appl. Catal. B* 221 (2018) 36–46.

[62] J.M. Cai, M.Q. Wu, Y.T. Wang, H. Zhang, M. Meng, Y. Tian, X.G. Li, J. Zhang, L.R. Zheng, J.L. Gong, *Chem.* 2 (2017) 877–892.

[63] L. Wang, J. Zhang, X.F. Wang, B.S. Zhang, W.J. Ji, X.J. Meng, D.S. Su, X.H. Bao, F.-S. Xiao, J. Mater. Chem. A Mater. Energy Sustain. 2 (2014) 3725–3729.

[64] Q.-N. Xia, Q. Cuan, X.-H. Liu, X.-Q. Gong, G.-Z. Lu, Y.-Q. Wang, *Angew. Chem. Int. Ed.* 53 (2014) 9755–9760.

[65] M. Kitano, K. Nakajima, J.N. Kondo, S. Hayashi, M. Hara, *J. Am. Chem. Soc.* 132 (2010) 6622–6623.

[66] X.B. Chen, S.H. Shen, L.J. Guo, S.S. Mao, *Chem. Rev.* 110 (2010) 6503–6570.

[67] H.J. Yu, R. Shi, Y.F. Zhao, G.I.N. Waterhouse, L.-Z. Wu, C.-H. Tung, T.R. Zhang, *Adv. Mater.* 28 (2016) 9454–9477.

[68] S. Fukuzumi, Y.-M. Lee, W. Nam, *Chem. Eur. J.* 24 (2018) 5016–5031.

[69] C.F. Zhang, Z.P. Huang, J.M. Lu, N.C. Luo, F. Wang, *J. Am. Chem. Soc.* 140 (2018) 2032–2035.

[70] X.K. Zeng, Z.Y. Wang, N. Meng, D.T. McCarthy, A. Deletic, J.H. Pan, X.W. Zhang, *Appl. Catal. B* 202 (2017) 33–41.

[71] R.R. Wang, K.C. Pan, D.D. Han, J.J. Jiang, C.X. Xiang, Z.Q. Huang, L. Zhang, X. Xiang, *ChemSusChem* 9 (2016) 2470–2479.

[72] S. Kato, J. Jung, T. Suenobu, S. Fukuzumi, *Energy Environ. Sci.* 6 (2013) 3756–3764.

[73] R.J. Lewis, J.K. Edwards, S.J. Freakley, G.J. Hutchings, *Ind. Eng. Chem. Res.* 56 (2017) 13287–13293.

[74] E.N. Ntainjua, M. Piccinini, S.J. Freakley, J.C. Pritchard, J.K. Edwards, A.F. Carley, G.J. Hutchings, *Green Chem.* 14 (2012) 170–181.

[75] S.J. Freakley, R.J. Lewis, D.J. Morgan, J.K. Edwards, G.J. Hutchings, *Catal. Today* 248 (2015) 10–17.

[76] H.E. Jeong, S. Kim, M.-G. Seo, D.-W. Lee, K.-Y. Lee, *J. Mol. Catal. A Chem.* 420 (2016) 88–95.

[77] B.-B. Gema, C.-S. Encarnación, M.C.M. Jose, J.L.G. Fierro, *Chem. Commun. (Camb.)* 10 (2004) 1184–1185.

[78] V.R. Choudhary, C. Samanta, *J. Catal.* 238 (2006) 28–38.

[79] C. Samanta, *Appl. Catal. B* 350 (2008) 133–149.

[80] H.-I. Kim, Y. Choi, S. Hu, W.Y. Choi, J.-H. Kim, *Appl. Catal. B* 229 (2018) 121–129.

[81] M. Teranishi, S.-I. Naya, H. Tada, *J. Phys. Chem. C* 120 (2016) 1083–1088.

[82] T. Zhou, Y.G. Xu, X. Wang, S.Q. Huang, M. Xie, J.X. Xia, L.Y. Huang, H. Xu, H.M. Li, *Catal. Sci. Technol.* 8 (2018) 551–561.

[83] G.-H. Moon, M. Fujitsuka, S. Kim, T. Majima, X.C. Wang, W.Y. Choi, *ACS Catal.* 7 (2017) 2886–2895.

[84] V. Peneau, G. Shaw, R.D. Armstrong, R.L. Jenkins, N. Dimitratos, S.H. Taylor, H.W. Zanthoff, S. Peitz, G. Stochniol, G.J. Hutchings, *Catal. Sci. Technol.* 6 (2016) 7521–7531.

[85] G.-H. Moon, W.Y. Kim, A.D. Bokare, N.-E. Sung, W.Y. Choi, *Energy Environ. Sci.* 7 (2014) 4023–4028.

[86] R.Z. Chen, J.J. Pignatello, *Environ. Sci. Technol.* 31 (1997) 2399–2406.